


## Article

# Relationship between Manufacturing and Properties of Vacuum Sintered Ti and Ti-6Al-7Nb

Leandro Bolzoni <sup>1,\*</sup> , Elisa Maria Ruiz-Navas <sup>2</sup> and Elena Gordo <sup>2</sup><sup>1</sup> School of Engineering, The University of Waikato, Private Bag 3105, Hamilton 3240, New Zealand<sup>2</sup> Department of Materials Science and Engineering, University Carlos III of Madrid, Avda. de la Universidad, 30, 28911 Leganes, Spain

\* Correspondence: bolzoni.leandro@gmail.com

**Abstract:** Titanium alloys are ideal for a great range of engineering applications; however, their high manufacturing costs hinder their widespread use. This study investigates the relationship between the processing and properties of representative Ti-based materials manufactured via powder metallurgy in order to reduce the manufacturing costs. This is possible as powder metallurgy techniques are near-net shape processes with high yield of material. It is found that the relative density increases with the sintering temperature, and it is slightly higher for longer processing times, reaching values in the 94–97% range. Moreover, homogeneous microstructures are obtained for all the conditions investigated, achieving an equiaxed microstructure for Ti and the typical lamellar structure for the Ti-6Al-7Nb alloy. However, the increment of the temperature also leads to a higher amount of interstitial pick-up, with a maximum increment of 0.21 wt.% and 0.028 wt.% for oxygen and nitrogen, respectively. The highest properties achieved for Ti and Ti-6Al-7Nb are 272 HV (hardness), 17.9 W/m·K (thermal conductivity), and 62.7 μohm·cm (electrical resistivity) and 336 HV, 6.9 W/m·K, and 180 μohm·cm, respectively.

**Keywords:** titanium alloys; powder metallurgy; blending elemental; homogeneous microstructure; sintering



**Citation:** Bolzoni, L.; Ruiz-Navas, E.M.; Gordo, E. Relationship between Manufacturing and Properties of Vacuum Sintered Ti and Ti-6Al-7Nb. *Alloys* **2022**, *1*, 232–242. <https://doi.org/10.3390/alloys1030014>

Academic Editor: Nikki Stanford

Received: 21 June 2022

Accepted: 25 August 2022

Published: 21 September 2022

**Publisher's Note:** MDPI stays neutral with regard to jurisdictional claims in published maps and institutional affiliations.



**Copyright:** © 2022 by the authors. Licensee MDPI, Basel, Switzerland. This article is an open access article distributed under the terms and conditions of the Creative Commons Attribution (CC BY) license (<https://creativecommons.org/licenses/by/4.0/>).

## 1. Introduction

Titanium (Ti), a lightweight metal with a density 40% lower than that of steel, is a relatively new engineering material with great potential for industrial applications, but whose employment has been limited by its peculiarities. On the one hand, Ti is characterized by a high chemical affinity for interstitial elements (i.e., oxygen, nitrogen, carbon, and hydrogen), which makes the extraction of Ti from its ores an expensive process, as the energy consumption to extract the same quantity of pure metal is 14 times higher than that needed for iron [1,2]. Moreover, the high chemical affinity leads to the need of using specialized manufacturing processes, which further increase the cost of Ti-based materials compared to competitor metals such as Al alloys [3,4]. On the other hand, Ti alloys are characterized by the highest relative mechanical performance (i.e., properties in relation to the density) as well as a good balance of properties including strength, toughness, and corrosion resistance. Consequently, the employment of Ti alloys has been strictly connected to the demand of high-performance industries such as the aeronautic sector [5,6], where the high final cost of Ti is not an issue.

Powder metallurgy (P/M) techniques are ideal methods to develop and process Ti alloys aiming to reduce the manufacturing costs and, therefore, expand the applicability of Ti to other industrial sectors. This is due to intrinsic advantages of P/M, including the reduced number of manufacturing operations needed to obtain the final product and the high material yield, meaning that the amount of expensive wasted material is minimized [7]. Cleaner and more reliable Ti powders are currently available due to the development of

new extraction/production methods, among which is the hydride–dehydride process [8], revitalizing industrial interest in manufacturing Ti alloys starting from powders.

Although in the literature the use of advanced P/M techniques such as equal channel angular pressure [9] and selective laser sintering [10] has been investigated, more conventional routes such as press and sinter still attract interest to minimize the manufacturing costs. This is confirmed by recent literature reviews on the properties of P/M Ti alloys [11,12], which highlight that most of the research effort on P/M of Ti is still focused on the Ti-6Al-4V alloy, whilst equivalent  $\alpha + \beta$  Ti alloys, which are the ones with the best strength/ductility pairs [13], have not been extensively researched, especially when processed via P/M. Specifically, the Ti-6Al-7Nb alloy is an  $\alpha + \beta$  Ti alloy with equivalent or better properties than Ti-6Al-4V [14,15], especially in terms of mechanical behavior and biocompatibility [16,17], and could therefore be used to replace the Ti-6Al-4V alloy if required, when cost is not an issue.

Regarding the addition of Al to Ti in binary Ti-Al alloys, Steedman et al. [18] investigated the influence of pure Al (Ti6Al) addition on the sintering behavior of P/M Ti using a blend compacted at room temperature. They found that the addition of the Al powder leads to a higher sintering rate compared to Ti. Bolzoni et al. [19] studied the influence of the addition of 1–6 wt.% of Al on the strengthening mechanisms of Ti produced via warm pressing plus vacuum sintering. It was found that the incremental addition of Al transforms the microstructure of Ti from equiaxed to coarse platelet Widmanstätten, resulting in the progressive strengthening via combined substitutional solid solution and grain boundary strengthening.

Concerning the addition of Nb to Ti, the main emphasis was to manufacture  $\beta$  Ti alloys (i.e., Nb  $\geq$  10 wt.%). For instance, Zhao et al. [20] manufactured Ti-xNb (x = 10, 16 and 22 wt.%) alloys through metal injection molding. Increasing the Nb content led to higher porosity, due to the slow diffusion of Nb, and the formation of  $\alpha + \beta$  Widmanstätten microstructures. By means of metal injection molding, Yilmaz et al. [21] fabricated Ti-xNb (x = 16, 28, 40 wt.%) alloys from Ti and Nb powders, finding that the increment of the Nb content causes a decrease in the hardness, bending strength, and elastic modulus of Ti-Nb alloys. Kalita et al. [22] considered Ti-xNb (x = 14, 20 and 26 wt.%) alloys produced by spark plasma sintering using high-purity Ti and Nb powders and annealed the sintered alloys at 1250 °C for 24 h, which was needed to fully dissolve the Nb powder particles.

The production of the Ti-6Al-7Nb alloys using P/M has been considered by Itoh et al. [16] using metal injection molding, and by Henriques et al. [15,17] by means of hot pressing. More recently, Hein et al. [23] analyzed the low cycle fatigue performance of the Ti-6Al-7Nb alloy obtained using laser powder bed fusion using a prealloyed Ti-6Al-7Nb powder. Cosma et al. [24] manufactured Ti-6Al-7Nb lattice structures via selective laser melting of a prealloyed Ti-6Al-7Nb powder. Similarly, Szymczyk et al. [25] used selective laser melting of a prealloyed Ti-6Al-7Nb powder to manufacture biomechanical functional structures. In terms of wrought Ti-6Al-7Nb alloy, Yu et al. [26] used equal channel angular pressing to obtain ultrafine-grained microstructures. Therefore, literature, especially recent, shows that the full potential of using conventional P/M routes to produce the Ti-6Al-7Nb alloy has not been fully explored.

Consequently, this work aims to identify the relationship between the processing parameters and the properties of representative Ti-based materials including Ti and the  $\alpha + \beta$  Ti-6Al-7Nb alloy. The processing is performed by means of the conventional P/M route, namely cold uniaxial pressing plus vacuum sintering, to limit manufacturing costs as much as possible. The properties of the sintered materials analyzed include physical, chemical, and mechanical properties as well as thermal conductivity and electrical resistivity, which are correlated with the processing parameters and the related microstructural features. It is worth noticing that the authors previously reported the manufacturing of the Ti-6Al-7Nb alloy studying the effect of the sintering temperature in the 700–1400 °C temperature range. Conversely to [27], the current study investigates the effect of a narrower sintering temperature range combined with the effect of the sintering time, which

has not been reported before. Specifically, different combinations of sintering parameters lead to different physical (i.e., relative density, porosity, etc.), mechanical (hardness), and microstructural properties (grain size, lamellar structure, porosity distribution, etc.), as well as different amounts of interstitial element pick-up, and this is clarified in the current work. Moreover, the understanding of the effect that different combinations of sintering parameters have on the thermal conductivity and electrical resistivity of P/M Ti and the Ti-6Al-7Nb alloy and the analysis of the expected variation of these properties on the basis of the nonlinear evolution of conductivity proposed in the literature is also studied.

## 2. Materials and Methods

The raw materials for the study were an irregularly shaped hydride–dehydride (HDH) Ti powder, obtained through a comminution process, a gas atomized spherical Al powder, and a crushed Ti:Nb:Al master alloy in powder form with angular morphology. Details of the method used to obtain the Ti-6Al-7Nb alloy using the master alloy addition approach are available in literature [28]. The Ti-based materials were cold pressed at 700 MPa by means of a uniaxial press, without holding time at the maximum pressure, using a zinc stearate die-wall lubricated floating die to produce rectangular shaped specimens. The green specimens were laid on zirconia balls and sintered in a high vacuum tubular furnace (approximately  $10^{-5}$  mbar) using a heating and cooling rate of 5 °C/min. The influence of the sintering temperature in the 1250–1350 °C window range was studied in combination with the effect of the processing time (i.e., 2 h and 4 h). It is worth mentioning that the selection of the pressing and sintering conditions was conducted based on common values used in the literature to process Ti alloys via P/M [29–33].

The density of the sintered samples was determined using the Archimedes method, and the relative density was calculated using the theoretical value of the wrought materials (4.51 g/cm<sup>3</sup> for pure Ti and 4.52 g/cm<sup>3</sup> for the Ti-6Al-7Nb alloy) [34]. The microstructure of the sintered samples was prepared following the classical metallographic route and the microconstituents revealed by etching with Kroll reactant. Microstructural analysis was carried out by means of an Olympus GX71 optical microscope and a Philips-XL30 scanning electron microscope operated at 20 KeV. Due to the great influence of interstitials on the mechanical properties of Ti and its alloys [35], the contents of oxygen and nitrogen by inert gas fusion technique were determined. Phase identification was performed through X-ray diffraction measurements in the 30–80° range by means of a Bruker AXS D8-Advance diffractometer equipped with a Cu K $\alpha$  radiation source. Vickers hardness (HV30) measurements were conducted by means of a Wilson Wolpert Universal Hardness DIGI-TESTOR 930 tester.

Thermal conductivity and electrical resistivity at room temperature were determined as a function of the sintering parameters. In particular, the thermal diffusivity of the samples was measured by means of a Netzsch LFA 447 Nanoflash equipment. Consequently, the thermal conductivity at room temperature was calculated on the basis of the relationship between the thermal conductivity ( $k$ ), the diffusivity ( $\alpha_d$ ), the relative density ( $\rho_r$ ), and the specific heat capacity at constant pressure ( $C_p$ ):  $k = \alpha_d \cdot \rho_r \cdot C_p$ . The electrical resistivity was determined on the basis of the measurement of the electrical conductivity performed by means of the van der Pauw methods [36,37].

## 3. Results

From Figure 1, the relative density of the sintered samples increases with the sintering temperature, ranging from 94.2% to 97.3%, and it is higher for longer dwell time. Consequently, the amount of porosity ranges from 2.7% to 5.8%, and it is lower for longer dwell times (Figure 1b). These are typical values for Ti alloys produced using the blending elemental approach [29–33]. Generally, there is a stronger effect from the processing temperature on the final density compared to the time, and the employment of a longer processing time is more beneficial for the Ti-6Al-7Nb alloy than for Ti.

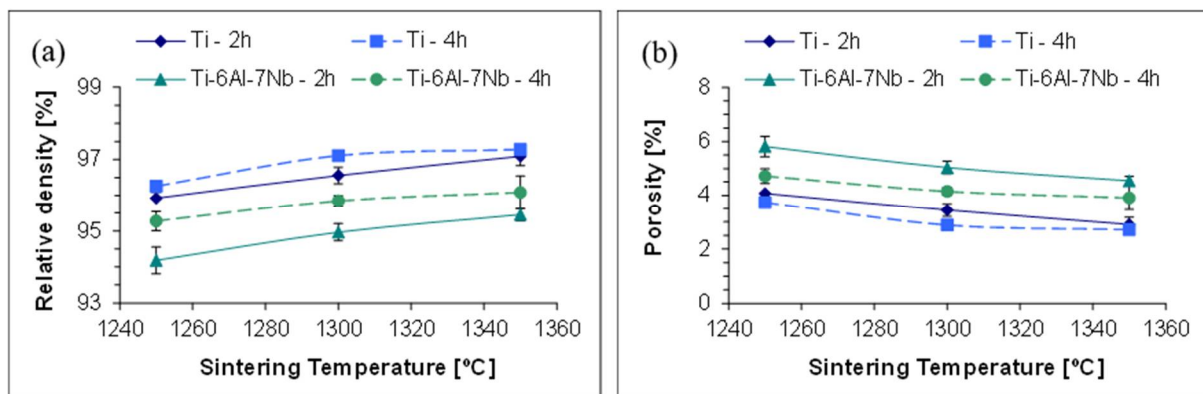


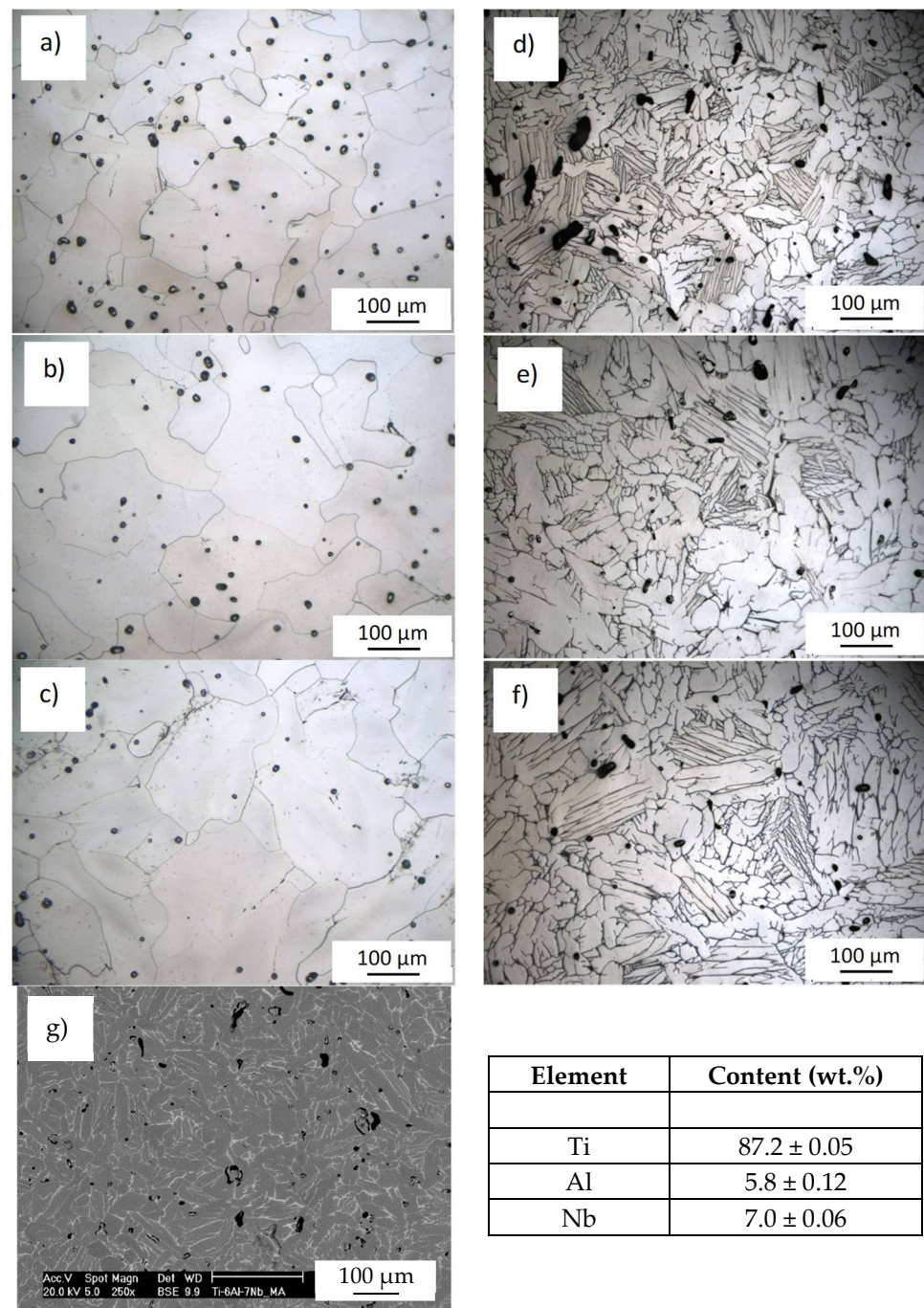
**Figure 1.** Variation of the relative density (a) and porosity (b) of the P/M Ti and Ti-6Al-7Nb alloy with the sintering temperature for different dwell times.

From the micrographs displayed in Figure 2, the microstructure of pure Ti is composed by alpha grains of different shape and size, and the materials experienced grain growth with either increasing the sintering temperature (Figure 2a compared to Figure 2b) or the processing time (Figure 2b compared to Figure 2c). Regarding the residual porosity, it is generally round-shaped, decreases in percentage, and grows in size with the sintering parameters. This is because starting from 94% of relative density, when the pore structure is composed of isolated pores, the pores tend to coalesce, reducing their amount but increasing their size. Specifically, the average pore size increases from  $12.4 \pm 2.3 \mu\text{m}$  to  $15.9 \pm 3.5 \mu\text{m}$  when the sintering temperature is increased from 1250 °C (Figure 2a) to 1350 °C (Figure 2b), and to  $19.4 \pm 1.8 \mu\text{m}$  when the dwell time is increased to 4 h (Figure 2c).

For the Ti-6Al-7Nb alloy, the residual porosity diminishes with the increment of the sintering temperature and time (Figure 1b), corresponding to a higher relative density, and becomes more spherical in shape. The microstructural constituents of the Ti-6Al-7Nb alloy are elongated alpha grains, whose size increases significantly with the processing temperature, and fine  $\alpha + \beta$  lamellae distributed throughout the microstructure (Figure 2 d–f). This is the typical lamellar microstructure of  $\alpha + \beta$  Ti alloys slow-cooled from a processing temperature above the  $\beta$  transus of the alloy [34,38,39]. It is worth mentioning that, with the selected processing conditions, completely homogeneous microstructures were obtained, as corroborated by SEM-EDS analysis (Figure 2g), as no undissolved powder particles were found in the sintered alloys. It is worth mentioning that for the sake of avoiding redundant data, only the SEM-EDS analysis of the Ti-6Al-7Nb alloy sintered at 1250 °C—2 h (i.e., lowest temperature and shortest time) are presented as representative.

Table 1 shows the results of the interstitial contents as measured in the sintered samples as well as the difference ( $\Delta$ ) compared to the starting powder (blend). It can be seen that, independently of the processing parameters employed, there is some oxygen and nitrogen pick-up with respect to the starting powders. Specifically, both oxygen and nitrogen percentages increase with the sintering temperature or the dwell time. Furthermore, the values of the interstitial contents are remarkably higher for the Ti-6Al-7Nb alloy with respect to pure Ti. It is worth mentioning that the actual composition of P/M Ti and Ti-6Al-7Nb alloy sintered in this study match the composition range specified for wrought Ti grade 4 and the wrought Ti-6Al-7Nb alloy, respectively (i.e., 5.5–6.5 wt.% Al and 6.5–7.5 wt.% Nb) [34]. However, the amount of oxygen of the sintered Ti-6Al-7Nb alloy is higher with respect to the limit indicated for the wrought Ti-6Al-7Nb alloy (i.e., 0.20 wt.% O and 0.05 wt.% N).

Figure 3 shows representative XRD patterns of the sintered Ti and Ti-6Al-7Nb alloy where it can be seen that the  $\alpha$ -Ti phase was exclusively detected in the case of Ti and both the  $\alpha$ -Ti and  $\beta$ -Ti phases were found for the Ti-6Al-7Nb alloy. The results show that only equilibrium phases were formed during the sintering and cooling of the selected Ti-based materials.

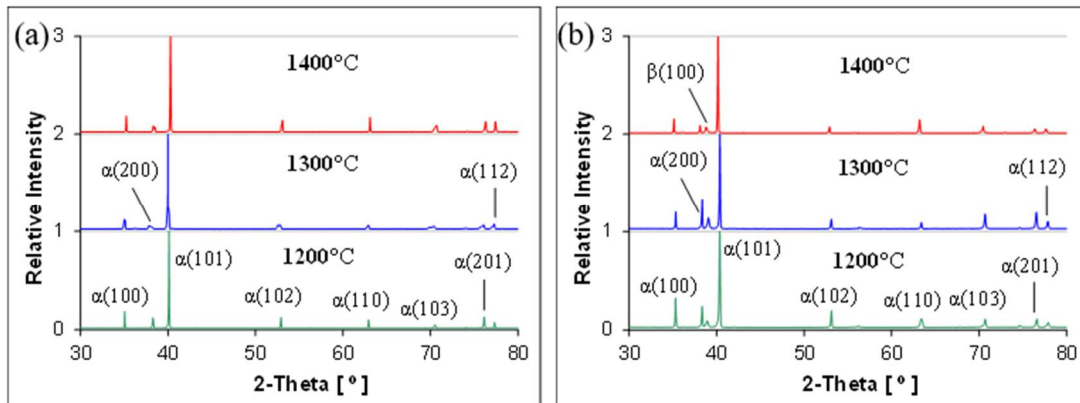
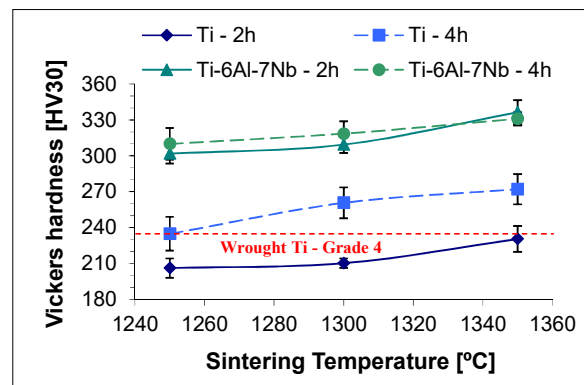


**Figure 2.** Representative optical micrographs of the P/M Ti (a–c) and Ti-6Al-7Nb (d–f) alloy: (a,d) 1250 °C—2 h, (b,e) 1350 °C—2 h, and (c,f) 1350 °C—4 h; and SEM micrograph (g) and related overall EDS chemical analysis of the Ti-6Al-7Nb alloy sintered at 1250 °C—2 h.

As for the relative density, the hardness of the materials studied (Figure 4) increases linearly with the sintering parameters, with higher hardness values for both higher temperatures and/or longer dwell times. For Ti, in most of the cases, the hardness values obtained are slightly lower compared to that of wrought Ti grade 4 [34]. Only the samples sintered at 1300 °C or 1350 °C for 4 h have Vickers hardness values equivalent or higher with respect to wrought Ti grade 4 in the annealed state [34], which is due to the high amount of interstitials dissolved. For the Ti-6Al-7Nb alloy, the hardness values are comparable to literature [40,41].

**Table 1.** Chemical analysis of the P/M Ti and Ti-6Al-7Nb alloy sintered using different combinations of sintering temperatures and dwell times.

Material	Conditions	Oxygen (wt.%)	$\Delta$	Nitrogen (wt.%)	$\Delta$
Ti	Starting powder	$0.27 \pm 0.01$	-	$0.016 \pm 0.003$	-
	1250 °C, 2 h	$0.32 \pm 0.01$	0.05	$0.020 \pm 0.004$	0.004
	1300 °C, 2 h	$0.33 \pm 0.04$	0.06	$0.025 \pm 0.006$	0.009
	1350 °C, 2 h	$0.38 \pm 0.01$	0.011	$0.024 \pm 0.004$	0.008
	1250 °C, 4 h	$0.36 \pm 0.02$	0.09	$0.028 \pm 0.006$	0.012
	1300 °C, 4 h	$0.41 \pm 0.04$	0.014	$0.044 \pm 0.008$	0.028
	1350 °C, 4 h	$0.41 \pm 0.06$	0.014	$0.042 \pm 0.004$	0.026
Ti-6Al-7Nb	Starting powder	$0.39 \pm 0.01$	-	$0.017 \pm 0.001$	-
	1250 °C, 2 h	$0.41 \pm 0.01$	0.02	$0.028 \pm 0.001$	0.011
	1300 °C, 2 h	$0.48 \pm 0.02$	0.09	$0.033 \pm 0.003$	0.016
	1350 °C, 2 h	$0.60 \pm 0.02$	0.021	$0.031 \pm 0.001$	0.014
	1250 °C, 4 h	$0.50 \pm 0.03$	0.011	$0.033 \pm 0.004$	0.016
	1300 °C, 4 h	$0.45 \pm 0.01$	0.06	$0.032 \pm 0.001$	0.015
	1350 °C, 4 h	$0.54 \pm 0.03$	0.015	$0.035 \pm 0.004$	0.018

**Figure 3.** Representative XRD patterns of the P/M Ti (a) and Ti-6Al-7Nb alloy (b).**Figure 4.** Variation of the Vickers hardness of the P/M Ti and Ti-6Al-7Nb alloy with the sintering temperature for different dwell times.

The values of the thermal conductivity and of the electrical resistivity are reported in Figure 5, where it can be seen that there are slight variations with the relative density. Thus, it can be stated that in the range of relative density between 94.2% and 97.3% (Figure 1), the decrement of the residual porosity is not crucial to improve the conductivity of P/M Ti-based materials, and comparable values to those of the respective wrought materials can be obtained. Moreover, the electrical resistivity of the sintered Ti-6Al-7Nb alloy is higher compared to the wrought alloy. It is worth mentioning that the expected variation

of thermal conductivity and electrical resistivity with the amount of residual porosity are schematically sketched as dashed black lines in Figure 5. The expected variation was estimated based on the nonlinear evolution of conductivity proposed by Vincent et al. [42].

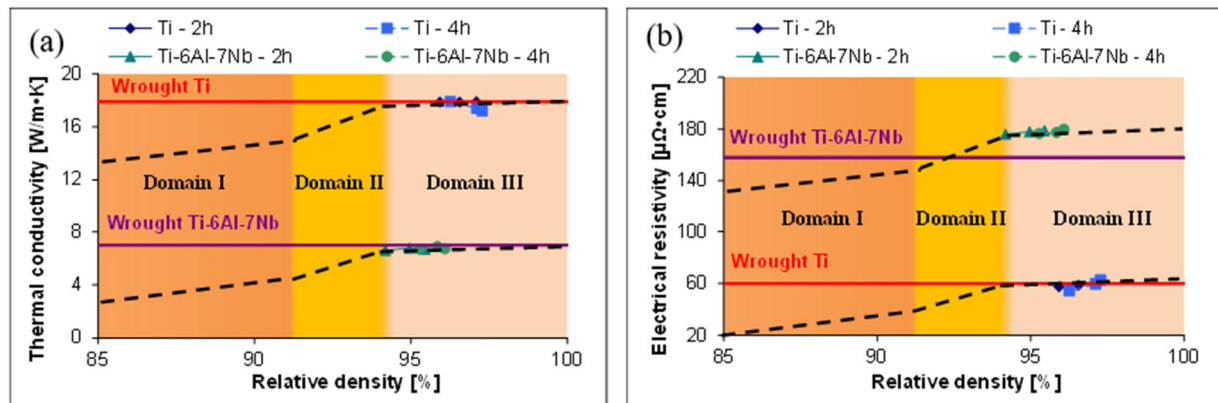


**Figure 5.** Variation of the thermal conductivity (a) and electrical resistivity (b) of the P/M Ti and Ti-6Al-7Nb alloy as a function of the relative density.

#### 4. Discussion

Manufacturing of Ti-based materials by means of uniaxial pressing plus vacuum sintering leads to a linear increment of the relative density. This is obviously related to the reduction in the surface area of the pressed powder particles. Therefore, the higher the temperature and the longer the dwell time, the higher the sintered density or, in turn, the lower the amount of residual porosity (Figure 1). However, the increment in terms of relative density obtained by doubling the sintering time from 2 h to 4 h does not justify the higher production cost associated and, thus, 2 h of sintering time is preferred.

By comparing the behavior of the two materials, it can be seen that they show similar increasing trends, but the final values obtained for the Ti-6Al-7Nb alloy are somewhat lower. Given that both of them were pressed uniaxially at 700 MPa and have equal green density (approximately 86%), the difference in terms of final relative density is due to the fact that part of the thermal energy supplied to the Ti-6Al-7Nb alloy is spent for diffusion and homogenization of the alloying elements instead of densifying the green compacts. The relative density values shown in Figure 1 are similar to the values available in the literature for Ti alloys produced using the blending elemental approach [29–33]. Specifically, Bolzoni et al. [19] obtained similar relative density values (i.e., 93–95%) when processing binary Ti-xAl alloys, and similarly Zhao et al. [20] achieved similar values (i.e., 94–96%) in binary Ti-xNb alloys.

The microstructural analysis performed on the sintered samples (Figure 2) shows that sintered Ti is composed of equiaxed grains, whilst the Ti-6Al-7Nb alloy has the typical lamellar structure composed of  $\alpha$  grains filled with parallel  $\alpha + \beta$  lamellae. The different orientation of the lamellae in different  $\alpha$  grains simply derives by the different orientations of the prior beta grains as well as by the fact that there are 12 possible orientation variations for the  $\alpha + \beta$  lamellae to nucleate from the prior  $\beta$  grains upon slow cooling. As it could be expected, the higher the sintered temperature and the longer the dwell time at maximum temperature, the coarser the microstructural features. Moreover, microstructural analysis reveals that the sintered Ti and Ti-6Al-7Nb alloy are characterized by isolated, spherical residual pores, which are primarily found at the grain boundaries.

Coherently with the results of the relative density, both the grain growth experienced and the fact that the pores are spherical and isolated confirm that, under the manufacturing conditions used, the sintered materials reached the third stage of sintering. Reaching the last stage of sintering is more critical for the Ti-6Al-7Nb alloy than for Ti, as dissolution and homogenization of the alloying elements added to create the Ti-6Al-7Nb alloy is required during sintering of the material. The homogenization of the chemistry can already be seen

from the micrographs of Figure 2, and it was confirmed via SEM-EDS analysis (Figure 2g). This indicates that the thermal energy supplied to the system is sufficiently high in order to promote the diffusion of the alloying elements towards the Ti matrix and to guarantee their homogenization. Comparable homogenization behavior and formation of lamellar microstructures was obtained during the sintering of binary Ti-xNb alloys from elemental powders [20–22].

The data of Table 1 clearly show that there is both oxygen and nitrogen pick-up during vacuum sintering. Generally, the higher the sintering temperature and the longer the dwell time at maximum temperature, the higher the interstitial pick-up compared to the starting powders [43]. This result reveals that the sintering step greatly influences the final amount of interstitials dissolved by Ti and the Ti-6Al-7Nb alloy, because it allows the elements adsorbed on the surfaces of the powder particles to diffuse inside the material. Furthermore, the higher interstitial pick-up of the Ti-6Al-7Nb alloy is related to the purity of the crushed Ti:Nb:Al master alloy used to obtain the Ti-6Al-7Nb alloy.

Figure 4 shows that the hardness increases linearly with the increase of the sintering temperature, and the hardness values are higher for longer dwell time at the maximum temperature. This is due to the combined effect of the reduction of the volume fraction of residual porosity and the increment of the interstitial elements due to the inward diffusion of oxygen and nitrogen during vacuum sintering. It is worth acknowledging that the grain growth obtained through higher sintering temperatures and longer sintering times is counteracting the two previously mentioned effects, reducing the hardness. Generally, sintered materials have similar trends in terms of relative density and hardness, and it is well known that interstitial elements such as oxygen and nitrogen harden Ti through interstitial solid solution strengthening [35]. It is interesting to note that, even though of the presence of the residual porosity (3–4%), the P/M Ti samples reach similar hardness values to wrought Ti grade 4 (253 HV) due to the amount of interstitials dissolved in them. However, in the majority of cases the hardness of the sintered Ti samples is lower compared to that of annealed wrought Ti [34]. The hardness values obtained for the P/M Ti-6Al-7Nb alloy samples are in between the hardness specified for the IMI 367 alloy (290 HV) [40] and that found in the wrought alloy by Semlitsch et al. (350 HV) [41]. Once again this is due to the balance between the amount of residual porosity and the contents of interstitial elements. For instance, Kalita et al. [22] achieved comparable hardness values (i.e., 303–325 HV) in spark-plasma-sintered binary Ti-Nb alloys.

The variation of the thermal conductivity and of the electrical resistivity of Ti and the Ti-6Al-7Nb alloy with the relative density (Figure 5) indicates that within the range of relative density values achieved, the progressive reduction of the residual porosity does not lead to a significant increment of the properties. This is mainly due to the fact that relative density values above 94% mean that the amount of porosity is below its percolation limit and, therefore, porosity is not the main contributing factor. The behavior found is in agreement with the discussion on the effect of porosity on the conductivity of copper processed by P/M reported by Vincent et al. [42], on which the authors identified three domains (sketched in Figure 5 as dashed black lines):

- Domain I (between 0 and 6% of porosity, i.e., 94–100%  $\rho_r$ ): linear decrease with porosity with low slope;
- Domain II (between 6 and 9%, i.e., 91–94%  $\rho_r$ ): steep decrease with porosity;
- Domain III (over 9%, i.e., below 91%  $\rho_r$ ): linear decrease with porosity with a slope larger than in Domain I.

The limited variations shown in Figure 5 are due to the counteracting effect of different aspects, including the different level of residual porosity present in each sample, porosity which is most likely filled with air and/or gas, and the specific characteristics of the microconstituents, i.e., alpha grains,  $\alpha + \beta$  lamellae, and volumetric percentage of grain boundaries, which generally coarsen with the increment of both sintering temperature and the dwell time.



## 5. Conclusions

This study demonstrates that by using irregular hydride–dehydride powders and the blended elemental approach, it is possible to obtain sintered Ti-based materials with relative densities between 94.2% and 97.3% and fully homogeneous microstructures. Specifically, an equiaxed microstructure composed of  $\alpha$  grains is obtained in Ti, and the typical lamellar structure composed of  $\alpha$  grains and  $\alpha + \beta$  lamellae is achieved in the Ti-6Al-7Nb alloy. The hardness increases with the sintering temperature and dwell time ranging from 206 HV to 272 HV in Ti and from 302 HV to 336 HV in the Ti-6Al-7Nb alloy. These values are similar to those of the respective wrought materials, even though of the presence of the residual porosity, due to the high amount of interstitials dissolved. Finally, this study also demonstrates that with the combination of sintering temperatures and dwell times employed, both thermal conductivity and electrical resistivity do not vary significantly, and the final values reached are similar to those of the respective wrought materials. In particular, the average thermal conductivity and electrical resistivity of the sintered Ti and Ti-6Al-7Nb alloys are 17.7 W/m·K and 58.8  $\mu\text{ohm}\cdot\text{cm}$  and 6.7 W/m·K and 177.9  $\mu\text{ohm}\cdot\text{cm}$ , respectively. The processing route analyzed is thus a promising alternative method to manufacture Ti-based materials of non-critical applications at lower cost.

**Author Contributions:** Conceptualization, L.B., E.M.R.-N. and E.G.; methodology, L.B.; formal analysis, L.B.; investigation, L.B.; resources, E.M.R.-N. and E.G.; data curation, L.B.; writing—original draft preparation, L.B.; writing—review and editing, L.B. All authors have read and agreed to the published version of the manuscript.

**Funding:** This research was funded by the New Zealand Ministry of Business, Innovation and Employment (MBIE) through the TiTeNZ (Titanium Technologies New Zealand—UOWX1402) research contract.

**Data Availability Statement:** All data pertaining to this work will be made available on request.

**Acknowledgments:** The authors want to acknowledge the financial support from the New Zealand Ministry of Business, Innovation and Employment (MBIE) through the TiTeNZ (Titanium Technologies New Zealand—UOWX1402) research contract.

**Conflicts of Interest:** The authors declare no conflict of interest.

## References

1. Crowley, G. How to Extract Low-cost Titanium. *Adv. Mat. Proc.* **2003**, *161*, 25–27.
2. Jackson, M.; Dring, K. Materials Perspective—A Review of Advances in Processing and Metallurgy of Titanium Alloys. *Mat. Sci. Technol.* **2006**, *22*, 881–887. [[CrossRef](#)]
3. Nowak, M.; Yeoh, W.K.; Bolzoni, L.; Babu, N.H. Development of Al-Nb-B Master Alloys using Nb and  $\text{KBF}_4$  Powders. *Mat. Des.* **2015**, *75*, 40–46. [[CrossRef](#)]
4. Bolzoni, L.; Nowak, M.; Babu, N.H. Assessment of the Influence of Al-2Nb-2B Master Alloy on the Grain Refinement and Properties of LM6 (A413) Alloy. *Mater. Sci. Eng. A* **2015**, *628*, 230–237. [[CrossRef](#)]
5. Allen, P. Titanium Alloy Development. *Adv. Mat. Proc.* **1996**, *150*, 35–37.
6. Froes, F.H. Titanium—Is the Time Now? *JOM* **2004**, *56*, 30. [[CrossRef](#)]
7. Bolzoni, L.; Ruiz-Navas, E.M.; Gordo, E. Influence of Vacuum Hot-pressing Temperature on the Microstructure and Mechanical Properties of Ti-3Al-2.5V Alloy Obtained by Blended Elemental and Master Alloy Addition Powders. *Mat. Chem. Phys.* **2012**, *137*, 608–616. [[CrossRef](#)]
8. Hurless, B.E.; Froes, F.H. Lowering the Cost of Titanium. *AMPTIAC Q.* **2002**, *6*, 3–10.
9. Lapovok, R.; Tomus, D.; Muddle, B. Low-temperature Compaction of Ti-6Al-4V Powder using Equal Channel Angular Extrusion with Back Pressure. *Mater. Sci. Eng. A* **2008**, *490*, 171–180. [[CrossRef](#)]
10. Song, B.; Dong, S.; Zhang, B.; Liao, H.; Coddet, C. Effects of Processing Parameters on Microstructure and Mechanical Property of Selective Laser Melted Ti6Al4V. *Mater. Des.* **2012**, *35*, 120–125. [[CrossRef](#)]
11. Kumar, P.; Chandran, K.S.R. Strength–Ductility Property Maps of Powder Metallurgy (PM) Ti-6Al-4V Alloy: A Critical Review of Processing–Structure–Property Relationships. *Met. Mater. Trans. A* **2017**, *48*, 2301–2319. [[CrossRef](#)]
12. Fang, Z.Z.; Paramore, J.D.; Sun, P.; Chandran, K.R.; Zhang, Y.; Xia, Y.; Cao, F.; Koopman, M.; Free, M. Powder Metallurgy of Titanium—Past, Present, and Future. *Int. Mat. Rev.* **2018**, *63*, 407–459. [[CrossRef](#)]
13. Raynova, S.; Imam, M.; Yang, F.; Bolzoni, L. Hybrid Microwave Sintering of Blended Elemental Ti Alloys. *J. Manuf. Process.* **2019**, *39*, 52–57. [[CrossRef](#)]

14. Itoh, Y.; Miura, H.; Uematsu, T.; Sato, K.; Niinomi, M. Improvement of the Properties of Ti-6Al-7Nb Alloy by Metal Injection Molding. In *Advances in Powder Metallurgy & Particulate Materials*; Metal Powder Industries Federation: Princeton, NJ, USA, 2007; pp. 52–57.
15. Henriques, V.A.; Bellinati, C.E.; da Silva, C.R. Production of Ti-6%Al-7%Nb Alloy by Powder Metallurgy (P/M). *J. Mat. Proc. Technol.* **2001**, *118*, 212–215. [[CrossRef](#)]
16. Itoh, Y.; Miura, H.; Sato, K.; Niinomi, M. Fabrication of Ti-6Al-7Nb Alloys by Metal Injection Molding. *Mater. Sci. Forum* **2007**, *534–536*, 357–360. [[CrossRef](#)]
17. Henriques, V.; Sandim, H.; Coelho, G.; da Silva, C. Microstructural Evolution during Hot Pressing of the Blended Elemental Ti-6%Al-7%Nb Alloy. *Mater. Sci. Eng. A* **2003**, *347*, 315–324. [[CrossRef](#)]
18. Steedman, G.; Corbin, S.F.; O'Flynn, J. Distinguishing the Influence of Aluminium and Vanadium Additions on Microstructural Evolution and Densification Behaviour during the Sintering of Ti6Al, Ti4V and Ti6Al4V. *Powder Metal.* **2018**, *61*, 301–312. [[CrossRef](#)]
19. Bolzoni, L.; Raynova, S.; Yang, F. Strengthening Mechanisms of Ti via Al Addition. *J. Alloys Compd.* **2020**, *820*, 153447. [[CrossRef](#)]
20. Zhao, D.; Chang, K.; Ebel, T.; Qian, M.; Willumeit, R.; Yan, M.; Pyczak, F. Microstructure and Mechanical Behavior of Metal Injection Molded Ti-Nb Binary Alloys as Biomedical Material. *J. Mech. Behav. Biomed. Mater.* **2013**, *28*, 171–182. [[CrossRef](#)]
21. Yılmaz, E.; Gökçe, A.; Findik, F.; Gulsoy, H. Metallurgical Properties and Biomimetic HA Deposition Performance of Ti-Nb PIM Alloys. *J. Alloys Compd.* **2018**, *746*, 301–313. [[CrossRef](#)]
22. Kalita, D.; Rogal, Ł.; Czeppe, T.; Wójcik, A.; Kolano-Burian, A.; Zackiewicz, P.; Kania, B.; Dutkiewicz, J. Microstructure and Mechanical Properties of Ti-Nb Alloys Prepared by Mechanical Alloying and Spark Plasma Sintering. *J. Mater. Eng. Perform.* **2020**, *29*, 1445–1452. [[CrossRef](#)]
23. Hein, M.; Kokalj, D.; Dias, N.F.L.; Stangier, D.; Oltmanns, H.; Pramanik, S.; Kietzmann, M.; Hoyer, K.-P.; Meißner, J.; Tillmann, W.; et al. Low Cycle Fatigue Performance of Additively Processed and Heat-Treated Ti-6Al-7Nb Alloy for Biomedical Applications. *Metals* **2022**, *12*, 122. [[CrossRef](#)]
24. Cosma, C.; Drstvensek, I.; Berce, P.; Prunean, S.; Legutko, S.; Popa, C.; Balc, N. Physical-Mechanical Characteristics and Microstructure of Ti6Al7Nb Lattice Structures Manufactured by Selective Laser Melting. *Materials* **2020**, *13*, 4123. [[CrossRef](#)]
25. Szymczyk, P.; Ziółkowski, G.; Junka, A.; Chlebus, E. Application of Ti6Al7Nb Alloy for the Manufacture of Biomechanical Functional Structures (BFS) for Custom-Made Bone Implants. *Materials* **2018**, *11*, 971. [[CrossRef](#)]
26. Yu, Z.; Dong, Y.; Li, X.; Niu, J.; Alexandrov, I.; Chang, H. Study on Corrosion Behavior of Ultrafine-Grained Ti-6Al-7Nb Fabricated by Equal Channel Angular Pressing. *Metals* **2020**, *10*, 950. [[CrossRef](#)]
27. Bolzoni, L.; Weissgaerber, T.; Kieback, B.; Ruiz-Navas, E.; Gordo, E. Mechanical Behaviour of Pressed and Sintered CP Ti and Ti-6Al-7Nb Alloy obtained from Master Alloy Addition Powder. *J. Mech. Behav. Biomed. Mater.* **2013**, *20*, 149–161. [[CrossRef](#)] [[PubMed](#)]
28. Bolzoni, L.; Ruiz-Navas, E.; Neubauer, E.; Gordo, E. Inductive Hot-pressing of Titanium and Titanium Alloy Powders. *Mater. Chem. Phys.* **2012**, *131*, 672–679. [[CrossRef](#)]
29. Ivasishin, O.M.; Anokhin, V.; Demidik, A.; Savvakina, D.G. Cost-Effective Blended Elemental Powder Metallurgy of Titanium Alloys for Transportation Application. *Key Eng. Mater.* **2000**, *188*, 55–62. [[CrossRef](#)]
30. Jia, M.; Gabbitas, B.; Bolzoni, L. Evaluation of Reactive Induction Sintering as a Manufacturing Route for Blended Elemental Ti-5Al-2.5Fe Alloy. *J. Mat. Proc. Technol.* **2018**, *255*, 611–620. [[CrossRef](#)]
31. Rock, B.; Imam, M.; Zarah, T. Microwave Assisted Sintering of Cold Iso-Statically Pressed Titanium 6-4 Powder Compacts. In *Processing, Properties, and Design of Advanced Ceramics and Composites*; John Wiley & Sons, Inc.: Hoboken, NJ, USA, 2016; pp. 213–221.
32. Bolzoni, L.; Ruiz-Navas, E.M.; Gordo, E. Investigation of the Factors Influencing the Tensile Behaviour of PM Ti-3Al-2.5V Alloy. *Mat. Sci. Eng. A* **2014**, *609*, 266–272. [[CrossRef](#)]
33. Kim, Y.; Lee, J.; Lee, B.; Ryu, H.J.; Hong, S.H. Dilatometric Analysis and Microstructural Investigation of the Sintering Mechanisms of Blended Elemental Ti-6Al-4V Powders. *Met. Mater. Trans. A* **2016**, *47*, 4616–4624. [[CrossRef](#)]
34. Boyer, R.; Welsch, G.; Collings, E.W. (Eds.) *Materials Properties Handbook: Titanium Alloys*, 2nd ed.; ASTM International: West Conshohocken, PA, USA, 1998.
35. Yan, M.; Xu, W.; Dargusch, M.S.; Tang, H.P.; Brandt, M.; Qian, M. Review of Effect of Oxygen on Room Temperature Ductility of Titanium and Titanium Alloys. *Powder Metal.* **2014**, *57*, 251–257. [[CrossRef](#)]
36. van der Pauw, L.J. A Method of Measuring Specific Resistivity and Hall Effect of Discs of Arbitrary Shape. *Philips Res. Rep.* **1958**, *13*, 1–9.
37. van der Pauw, L.J. A Method of Measuring Specific Resistivity and Hall Effect on Lamellae of Arbitrary Shape. *Philips Technol. Rev.* **1958**, *20*, 220–224.
38. Luo, S.; Yang, Y.; Schaffer, G.; Qian, M. Warm Die Compaction and Sintering of Titanium and Titanium Alloy Powders. *J. Mater. Process. Technol.* **2014**, *214*, 660–666. [[CrossRef](#)]
39. Bolzoni, L.; Alqattan, M.; Peters, L.; Alshammari, Y.; Yang, F. Ternary Ti Alloys Functionalised With Antibacterial Activity. *Sci. Rep.* **2020**, *10*, 22201. [[CrossRef](#)]
40. Henry, D. *Materials and Coatings for Medical Devices: Cardiovascular*; ASTM International: West Conshohocken, PA, USA, 2009.

41. Semlitsch, M.; Weber, H.; Steger, R. Fifteen Years Experience with Ti-6Al-7Nb Alloy for Joint Replacements. In *Titanium '95: Science and Technology, Proceedings of the Eighth World Conference, Birmingham, UK, 22–26 October 1995*; Institute of Materials: Singapore, 1996.
42. Vincent, C.; Silvain, J.; Heintz, J.; Chandra, N. Effect of porosity on the thermal conductivity of copper processed by powder metallurgy. *J. Phys. Chem. Solids* **2012**, *73*, 499–504. [[CrossRef](#)]
43. Raynova, S.; Collas, Y.; Yang, F.; Bolzoni, L. Advancement in the Pressureless Sintering of CP Titanium Using High-Frequency Induction Heating. *Met. Mater. Trans. A* **2019**, *50*, 4732–4742. [[CrossRef](#)]